

Analytical process model for wire + arc additive manufacturing

Sergio Ríos^{a,b,*}, Paul A. Colegrove^a, Filomeno Martina^a, Stewart W. Williams^a

^a Cranfield University, University Way, Cranfield, Bedfordshire MK43 0AL, UK

^b University of Magallanes, Manuel Bulnes 01855, Punta Arenas, Región de Magallanes y La Antártica Chilena, Chile

ARTICLE INFO

Keywords:

Wire + arc additive manufacture

Welding capillarity

Point source conduction

ABSTRACT

An analytical process model for predicting the layer height and wall width from the process parameters was developed for wire + arc additive manufacture of Ti-6Al-4V, which includes inter-pass temperature and material properties. Capillarity theory predicted that cylindrical deposits were produced where the wall width was less than 12 mm (radius < 6 mm) due to the large value of the surface tension. Power was predicted with an accuracy of $\pm 20\%$ for a wide range of conditions for pulsed TIG and plasma deposition. Interesting differences in the power requirements were observed where a surface depression was produced with the plasma process due to differences in melting efficiency and/or convection effects. Finally, it was estimated the impact of controlling the workpiece temperature on the accuracy of the deposit geometry.

1. Introduction

Additive Manufacture (AM) is a recent fabrication technology, which consists of building parts by consecutively depositing layers of material, onto a substrate. Wire + arc additive manufacture (WAAM) is a variant of AM, currently under development at Cranfield University, which is based on welding processes such as metal inert gas and plasma welding [1]. This process can provide significant reductions in the material required to produce a part which reduces cost, as well as shortening lead times.

When producing a part, the main geometrical parameters to control are the effective wall width and the layer height (Fig. 1). These dimensions are inherited from the weld pool, in a similar fashion as the weld reinforcement in a welded seam. They result from the interaction between power from the arc, travel speed, deposition rate, inter-pass temperature and material properties.

When modelling welding processes, the weld pool dimensions can be calculated from the temperature field in a semi-infinite solid, around a moving point heat source. Analytical solutions to this problem were developed by Rosenthal [2] and Rykalin [3] and the problem is simplified by ignoring phase transformations and the temperature dependence of the physical properties. Eq. (1) shows the 2D version of this model, where the variables are net power input \dot{Q} , travel speed TS , plate thickness t , pre-heat temperature T_o , specific heat capacity C_p and thermal diffusivity α . $K_0()$ is the Bessel function of the first kind and zero order.

$$T - T_o =$$

$$\frac{\dot{Q}}{2\pi C_p t} \exp\left(-\frac{x}{L_c}\right) K_0\left(\frac{r_{xy}}{L_c}\right),$$

$$\text{where } L_c = \frac{2\alpha}{TS},$$

$$r_{xy} = \sqrt{x^2 + y^2}$$

(1)

The 2D version applies where the temperature field does not change significantly through the thickness [4]. This condition has been observed in thin plate welding and laser and electron beam welding of thick plates [5]. Fig. 2 illustrates the weld pool profile, which is determined by substituting T by the melting point T_m , in Eq. (1). The length Y_{max} is half the weld width.

When compared with experimental data, the point source models (2D and 3D) predict the area of the fusion zone and heat affected zone (HAZ) well; however, the weld pool width and length are predicted less accurately [6–14]. This shows the relative importance of conduction for predicting the HAZ and convection for the size of the weld pool, as Fuerschbach showed in [15].

Wells [16] extended the model presented by Rosenthal [2] to determine the weld power from the weld pool dimensions. Two forms of the equation were developed, and the simplified version is shown below:

$$\dot{Q} = 8k \cdot t \cdot (T_m - T_o) \cdot \left(\frac{1}{5} + \frac{Y_{max}}{L_c} \right)$$

(2)

This applies when the dimensionless parameter Y_{max}/L_c is greater than 0.1, and it predicts the power to within -6% and $+1\%$ compared

* Corresponding author at: University of Magallanes, Manuel Bulnes 01855, Punta Arenas, Región de Magallanes y La Antártica Chilena, Chile.
E-mail address: sergio.rios@umag.cl (S. Ríos).

List of symbols

α	thermal diffusivity
γ	surface tension
θ	layer angle
κ^{-1}	capillary radius
ρ	density
aWD'	apparent weld pool depth
aWD	apparent weld pool depth, corrected
c	compensation
C	mean curvature
CP	capillary pressure
C_p	specific heat capacity
CSA	layer cross section area
EWV	effective wall width
g	acceleration of gravity
h	hydrostatic height

HP	hydrostatic pressure
LH	layer height
\dot{Q}	net power into the material
R	remelting
r	layer radius
r_h	horizontal radius
r_v	vertical radius
r_{xy}	modulus of vector (x, y)
t	plate thickness
T	temperature at point (x, y)
T_o	inter-pass temperature
T_m	melting point
TS	travel speed
WFS	wire feed speed
WW	wall width
Y_{max}	half the weld pool width

to the original version.

Various models have been developed for predicting the weld pool dimensions in additive manufacture. Analytical models have been applied to AM by Pinkerton and Li [17] who used a simplified form of Rosenthal's model which was applicable to low travel speeds, while Beuth et al. [18] predicted molten pool length in AM.

The theoretical models by Pinkerton and Li [17], Shan [19] and Soylemez et al. [20] showed that the filler wire has little impact in the amount of energy required to form the weld pool. However, other researchers found that the temperature field within the molten pool is affected by the wire, which in turn changes the flow patterns and eventually the shape at the bottom of the weld pool [12,13].

More recently, Martina [21,22] developed empirical models, for Tungsten Inert Gas (TIG) and plasma WAAM. These models relate process parameters (*Current*, *TS*, *WFS*) and physical parameters (heat input, *WFS/TS* ratio), with *WW* and *LH*. A more general model for WAAM, including inter-pass temperature and material properties has not yet been developed.

The shape of a molten pool surface can be determined from the forces acting upon it [23–25]. The simplest possible analysis is the static case of a sessile drop, with only two forces, as shown in Fig. 3: the force due to hydrostatic pressure (*HP*) and the force due the capillary pressure (*CP*). Their values are given by Eqs. (3) and (4), as functions of the density (ρ), the gravitational acceleration (g), the height of the liquid column above the point of interest (h), the surface tension (γ) and the curvature of the surface (C).

$$HP = \rho \cdot g \cdot h \quad (3)$$

$$CP = \gamma \cdot C \quad (4)$$

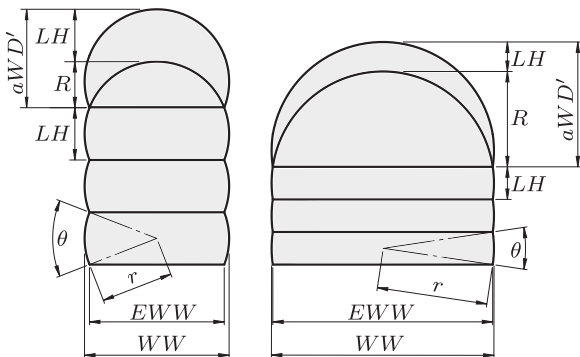


Fig. 1. Elements of the layer geometry in cross section, with the same amount of material per layer.

Although the shape of any weld pool generally differs from that of a sessile drop, the static analysis has been successfully applied by previous authors, under a clever approximation. The approximation used by Voloshkevich [26] and Berezovskii [27] was that of a prismatic liquid body, where one of the main curvatures is zero and the other one is found in the cross sectional profile of the weld. The differential definition of surface curvature allowed the authors to calculate the profile of reinforcements and fillet welds. From this, Voloshkevich [26] found that the interface property called capillary radius κ^{-1} (Eq. (5)) is a determining factor.

$$\kappa^{-1} = \sqrt{\frac{\gamma}{\rho \cdot g}} \quad (5)$$

The same assumption allowed Berezovskii [27] to predict the shape of weld reinforcements even when they are not of circular cross section. The prismatic approximation has yielded good results for predicting the shape of weld profiles, because towards the rear zone of the weld pool, far from the arc, *HP* and *CP* are indeed the main pressures acting on the surface.

2. Method

The model proposed here was built upon previous experimental data, in two stages. The first one is a study of the layer geometry, which results in a relationship between deposit and weld pool dimensions, of the same sort as the prismatic approximation referred to above. The second is the adaptation of Wells' simplified model to relate net power input to the deposit dimensions. This thermo-capillary model is then compared with the experimental data and used to assess the effect of process parameters on deposit dimensions.

Two sets of experiments involving Ti-6Al-4V provided the input data and in both cases the parameters were defined using a D-Optimal design of experiments [22]. The first set (Table 1a) corresponds to 17 deposits made with pulsed-TIG WAAM [22], 4 of which were duplicates. The experimental variables were average current, travel speed

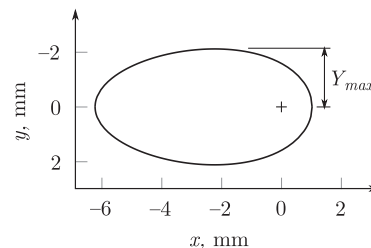


Fig. 2. Weld pool profile according to Rosenthal's model.

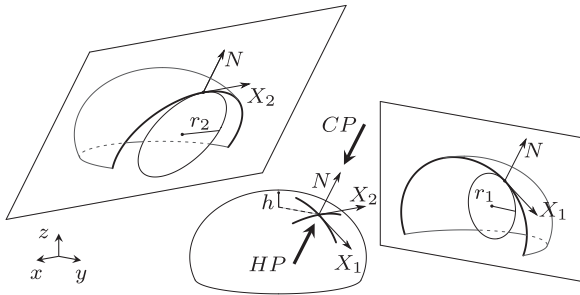


Fig. 3. A molten pool surface under the action of capillary pressure and hydrostatic pressure.

Table 1

Experimental variables of P-TIG and PTA experiments.

	Min	Max
(a) P-TIG		
Average current, A	120	220
Travel speed, mm s ⁻¹	2	6
Wire feed speed, m min ⁻¹	1.2	4
(b) PTA		
Diffuser length, mm	0.8	2.4
Diffuser angle, °	36.8	90.0
Current, A	100	229
Plasma gas flow rate, L min ⁻¹	0.80	5.00

and wire feed speed. Unfortunately, the arc voltage was not recorded, only monitored so a constant value of 12 V was used to determine the arc power. The second set of experiments (Table 1b) consisted of 25 deposits made with plasma deposition. The experimental variables were the nozzle design (diffuser length and angle), the current and the plasma gas flow rate. The travel and wire feed speeds were held constant and had values of 5 mm s⁻¹ and 50 mm s⁻¹ respectively.

2.1. Layer geometry in WAAM

Fig. 1 shows two WAAM deposits in cross section, identifying their main dimensions. The layer height LH , wall width WW and effective wall width EWW have been referred to by other authors [22,28]. The re-melting R , the apparent weld pool depth aWD' , the radius r and the angle θ are new features. Some images from plasma deposition are shown in Fig. 4, which show the LH and R as well as how the arc affects the front more than the rear of the weld pool.

The last deposited layer was analysed to determine how the geometry compared with a perfect circle. To do this, the horizontal r_h and

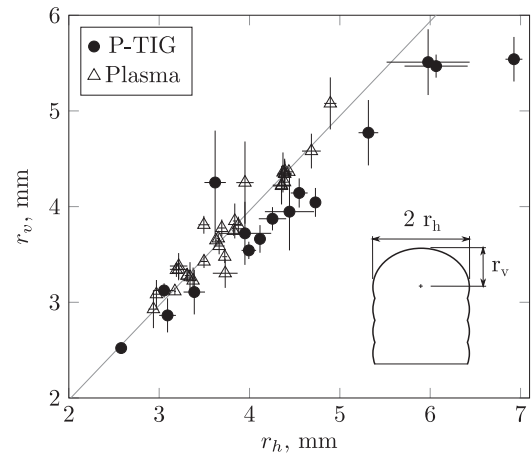


Fig. 5. Plot of the horizontal and vertical radii. Note that the error bars correspond to the standard deviation of the measurements.

vertical r_v , radii were measured and plotted against each other as shown in Fig. 5. The TIG samples were measured by metallographic analysis with 3 measurements per sample and the plasma samples were measured with a coordinate measurement machine, with 10 measurements per sample, along the direction of deposition. This plot shows that r_v and r_h are nearly identical in size for most deposits apart from those that are very large ($r_h > 6$ mm), where gravity causes the horizontal radius to exceed the vertical. This is similar to the transition from a sessile drop to a puddle, as the amount of liquid increases [24]. Therefore for radii less than 6 mm the layer shape can be assumed cylindrical. With this assumption the dimensions shown in Fig. 1 are parametrised in terms of r and θ , using Eqs. (6)–(10).

$$WW = 2r \quad (6)$$

$$LH = 2r \cdot \sin\left(\frac{\theta}{2}\right) \quad (7)$$

$$EWW = 2r \cdot \cos\left(\frac{\theta}{2}\right) \quad (8)$$

$$R = r \cdot \left(1 - \sin\left(\frac{\theta}{2}\right)\right) \quad (9)$$

$$aWD' = LH + R \quad (10)$$

Furthermore, the cross sectional area is given by:

$$CSA = r^2 \cdot (\theta + \sin(\theta)) \quad (11)$$

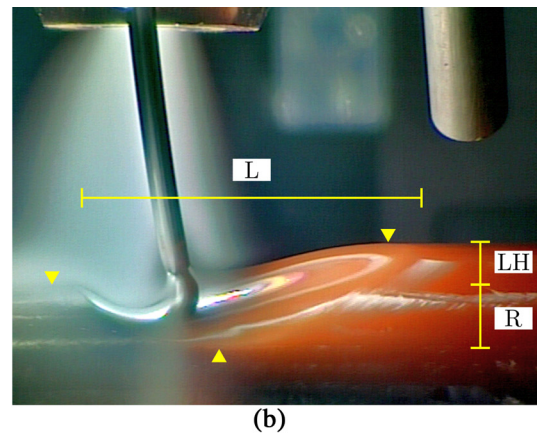
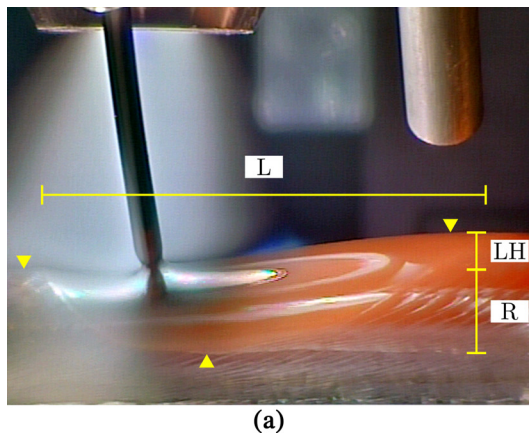


Fig. 4. Different thermal efficiency to produce the same deposit geometry in plasma WAAM, with (a) high and (b) low arc powers. Notice how the arc affects the front more than the rear of the weld pool.

From these equations, two more expressions can be derived.

$$LH = WW - 2 \cdot R \quad (12)$$

$$aWD' = \frac{WW + LH}{2} \quad (13)$$

Eqs. (12) and (13) represent the relationship between final dimensions of a deposit and the weld pool features. There is however one last geometrical construct, to compensate for the different geometry between the flat edge in Wells' model and the curved cross section of a WAAM deposit. This compensation c is shown in Fig. 6 and it reduces the value of aWD' , to match the area of the upper semicircle with a rectangle of base $2r$, so that

$$2r \cdot (r - c) = 0.5\pi r^2, \quad (14)$$

which then leaves

$$c = r \cdot \left(1 - \frac{\pi}{4}\right) \quad (15)$$

Thus the weld pool depth in this model is represented by

$$aWD = aWD' - c \quad (16)$$

Now, capillarity theory is applied to the cylindrical Ti-6Al-4V deposits. To ensure that the cylindrical approximation holds, $HP < CP$. The mean curvature of a cylinder is the reciprocal of its radius, which allows the capillary pressure (Eq. (4)) to be determined. Furthermore, the hydrostatic pressure, HP can be found by substituting $h = aWD'$, into Eq. (3), so the criterion for a cylindrical deposit can be expressed as:

$$r \cdot \sqrt{1 + \sin\left(\frac{\theta}{2}\right)} \leq \kappa^{-1}, \quad (17)$$

which is equivalent to

$$\frac{1}{2} \cdot WW \cdot \sqrt{1 + \frac{LH}{WW}} \leq \kappa^{-1} \quad (18)$$

The capillary radius κ^{-1} , as defined in Eq. (5), is calculated from physical properties. According to Wunderlich [29], the surface tension of Ti-6Al-4V, with low oxygen, at a temperature near melting point is $1.52 \pm 0.03 \text{ N m}^{-1}$, which results in $\kappa^{-1} = 5.9 \text{ mm}$. Hence, this criterion explains the reason why the cylindrical approximation breaks down for radii above 6 mm in Fig. 5. According to de Gennes et al. [24], above $r_h = \kappa^{-1}$, the sessile drop becomes a puddle and r_v remains constant at $r_v = \kappa^{-1}$.

2.2. Heat conduction model

These inequalities ((17) and (18)) represent the combinations of (r , θ) and (WW , LH) where the cylindrical approximation is valid. Layers whose dimensions are beyond this boundary are less likely to have a circular cross section. Furthermore, we can provide another criterion based on the deposition efficiency (ratio between the theoretical useful cross sectional area and the total cross sectional area) which is a reflection of the surface roughness:

$$\eta_{\text{dep}} = \frac{LH \cdot EWW}{CSA} \quad (19)$$

If we require this to be greater than 90%, then $LH < WW/2$. Both these inequalities are plotted in Fig. 7 against the experimental data points for layer height and wall width. The region in grey shows where both criteria are met and it is only the experimental data points where the radii exceed 6 mm which fall outside this region.

These relationships are now applied to Wells' model (Eq. (2)) which will be modified to represent the WAAM process instead of an autogenous weld on a thin plate. The main difficulty lies in the differences between both processes: WAAM is comparable to an edge weld, with filler material, whereas Wells' model refers to an autogenous weld on

an infinite plate. However, Shan et al. [19] showed that there is no significant difference in the heat input and conduction losses between the two scenarios. To allow WAAM to be modelled with this approach, the coordinate system and main dimensions are shown in Fig. 8 against the equivalent for an autogenous weld.

The following substitutions are made to allow Eq. (2) to be used:

$$t = EWW \quad (20)$$

$$\dot{Q}_{\text{plate}} = 2 \cdot \dot{Q}_{\text{wall}} \quad (21)$$

$$Y_{\text{max}} = aWD \quad (22)$$

The Wells' model uses constant values of conductivity, specific heat and density. In reality, these parameters are temperature dependent and are given by equations in McAndrew [30]. To simplify application of the model, temperature independent values were used which was an adjustable parameter in the model. The properties were chosen at 1600 K which reduced the error to the minimum. The values are $k = 24.0 \text{ W m}^{-1} \text{ K}^{-1}$; $C_p = 700 \text{ J kg}^{-1} \text{ K}^{-1}$ and $\alpha = 7.79 \times 10^{-6} \text{ m}^2 \text{ s}^{-1}$. After applying these substitutions, the model for additive manufacture takes the form shown:

$$\begin{aligned} \dot{Q}_{WAAM} = & 4k \cdot EWW \\ & (T_m - T_0) \left(\frac{1}{5} + \frac{aWD}{L_c} \right), \\ \text{where } L_c = & \frac{2\alpha}{TS} \end{aligned} \quad (23)$$

This presentation of the model does not explicitly include the wire feed speed or the layer height. However, in the absence of spatter and severe metal evaporation, WFS , TS and CSA are related through Eq. (24), which expresses the conservation of mass between the wire added and the deposit geometry. Here, A_{wire} represents the cross sectional area of the wire.

$$WFS \cdot A_{\text{wire}} = TS \cdot CSA \quad (24)$$

From a practical perspective, it is desirable to choose EWW and LH and then calculate the values of the process parameters. This is done with the following algorithm:

1. Calculate θ and r from Eqs. (7) and (8) and.
2. Verify that Inequality (17) holds. If it does not hold, choose a different combination of EWW and LH .
3. Calculate CSA from Eq. (11).
4. Choose TS and WFS from Eq. (24), considering equipment capabilities and productivity goals.
5. Calculate WW from Eq. (6).
6. Calculate aWD from Eqs. (13) and (16).
7. Calculate \dot{Q}_{wall} from Eq. (23).
8. Set the welding equipment to match \dot{Q}_{wall} , based on arc efficiency. If the equipment cannot produce \dot{Q}_{wall} as required, adjust WFS and/or TS at step 4 and try again.

To evaluate process robustness, the change in EWW and LH due to

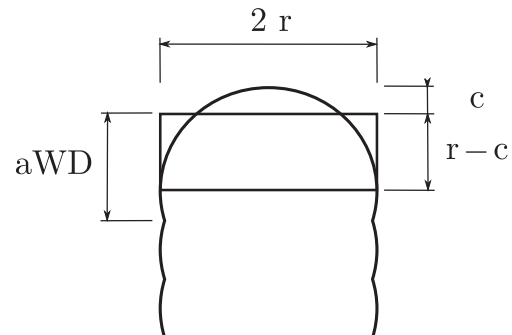


Fig. 6. Compensation for round shape in heat conduction model.

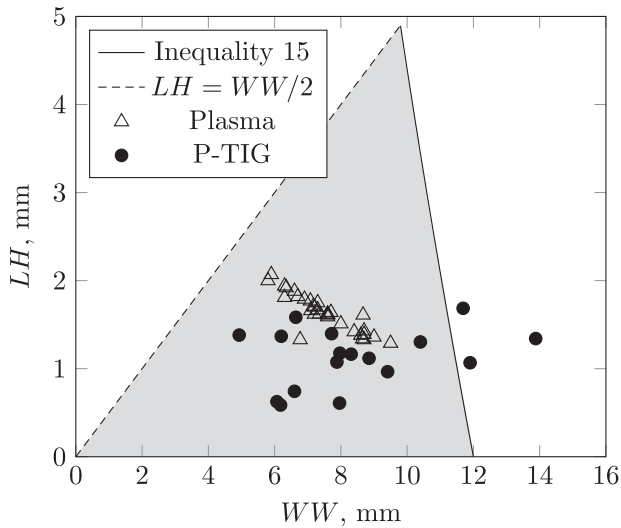


Fig. 7. Wall width and layer height vs. the criterion for a cylindrical deposit and deposition efficiency greater than 90%.

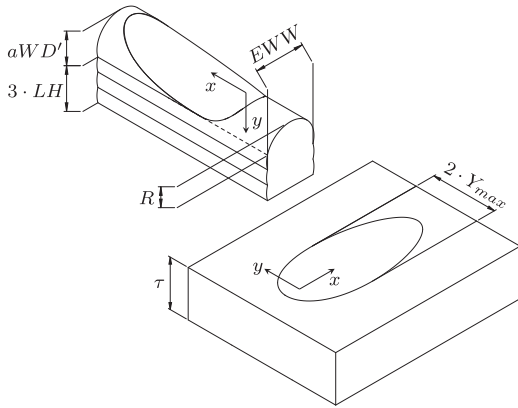


Fig. 8. Coordinate system and main geometric parameters for applying the 2D analytical model to (a) WAAM and (b) welding.

Table 2
Parameters for the sensitivity study.

	Min	Max
Net power input, W	734	2076
Travel speed, mm s ⁻¹	2	6
Wire feed speed, m min ⁻¹	1.2	4
Inter-pass temperature, K	373	673

10% increase in the four main process parameters: T_o , Q_{waam} , TS and WFS were determined. The sensitivity analysis was performed on the same set points used in the P-TIG experiments, with inter-pass temperature of 373 K and 673 K, which in total is 26 set points, after removing the duplicates. The parameter ranges are shown in Table 2. Only those points were the capillarity criterion (Inequality (18)) held were included in the analysis, i.e. 18 points for the sensitivity to changes in T_o and Q_{waam} , and 20 points for TS and WFS .

3. Results

The predicted \dot{Q}_{wall} is compared to experimental power input, with arc efficiencies of 70% and 45% for P-TIG and plasma respectively, according to [31,32]. Unfortunately, the present work lacks the calorimetric information of arc efficiency for these particular settings.

Nevertheless, the substitutions above result in reasonable agreement with experimental data, as shown in Fig. 9a and b. The error relative to the experimental values (Fig. 9c and d) shows that this WAAM model is able predict power within $\pm 20\%$.

Fig. 10 shows the relative change in deposit dimensions, due to a 10% increase in each process parameter, as an average over the 28 set points described at the end of Section 2. In most cases, the change in deposit dimensions is smaller than the change in process parameters, except the change in LH when the WFS varied. In this case, the relative change is the same. The sensitivity of the outputs varied little with the set points, as demonstrated by the small error bars, except the sensitivity with respect to T_o .

4. Discussion

4.1. Model performance

The analytical model developed in this study has enabled the power to be predicted within $\pm 20\%$ for a variety of experimental conditions in pulse TIG and plasma WAAM (Fig. 11). Furthermore, the model facilitates understanding of the effect of the input parameters (Fig. 10).

The sensitivity study whose results are plotted in Fig. 10 showed the effect of the main input parameters on the EWW and LH . It is easy to control power, travel speed and WFS relatively accurately during the process, however controlling the inter-pass temperature is far more difficult and is dependent on the size of the component, which affects the time between passes as well as the overall heat build-up. Therefore, it is quite easy to get over 100 K difference in the workpiece temperature, (larger than 30% of room temperature) which could have a significant effect on layer geometry. This could be compensated with a control system that adjusted the power accordingly and could negate the effect of workpiece temperature variations. Finally, one interesting observation from Fig. 10 is that the WFS almost does not affects the EWW , because the process power and travel speed determine the EWW due to heat conduction, within the operational envelope considered. To understand why this is the case, aWD from Eqs. (13) and (16) and $WW \approx EWW$ are substituted into Eq. (23) to give:

$$\begin{aligned} \dot{Q} &\approx 4k \cdot EWW (T_m - T_o) \\ &\quad \left(\frac{1}{5} + \frac{\frac{\pi}{2} \cdot EWW + LH}{2L_c} \right) \\ \dot{Q} &\approx 4k \cdot (T_m - T_o) \\ &\quad \left(\frac{EWW^2 + \frac{\pi}{2} \cdot EWW \cdot LH}{2L_c} \right) \\ \dot{Q} &\approx \rho C_p \cdot (T_m - T_o) \cdot TS \\ &\quad \cdot EWW^2 \left(1 + \frac{\pi}{2} \cdot \frac{LH}{EWW} \right) \end{aligned} \quad (25)$$

This equation shows that there is a very strong correlation between the parameters of heat conduction (\dot{Q} , C_p , TS) and the EWW due to the squared term. On the contrary, the layer height has a relatively small effect on the heat transfer and is therefore primarily related to the amount of wire going into the molten pool.

4.2. Thermal efficiency

Obviously, the 2D point source model is not meant to represent weld pools where convection is significant, as observed by a number of authors [12,31]. Convection can affect the amount of re-melted workpiece and overall thermal efficiency. In this study, a constant arc efficiency has been used when comparing the experimental and predicted power inputs in Fig. 9. In practice, the arc efficiency will depend on the current, plasma gas flow-rate, travel speed and whether the arc is pulsing or not [31].

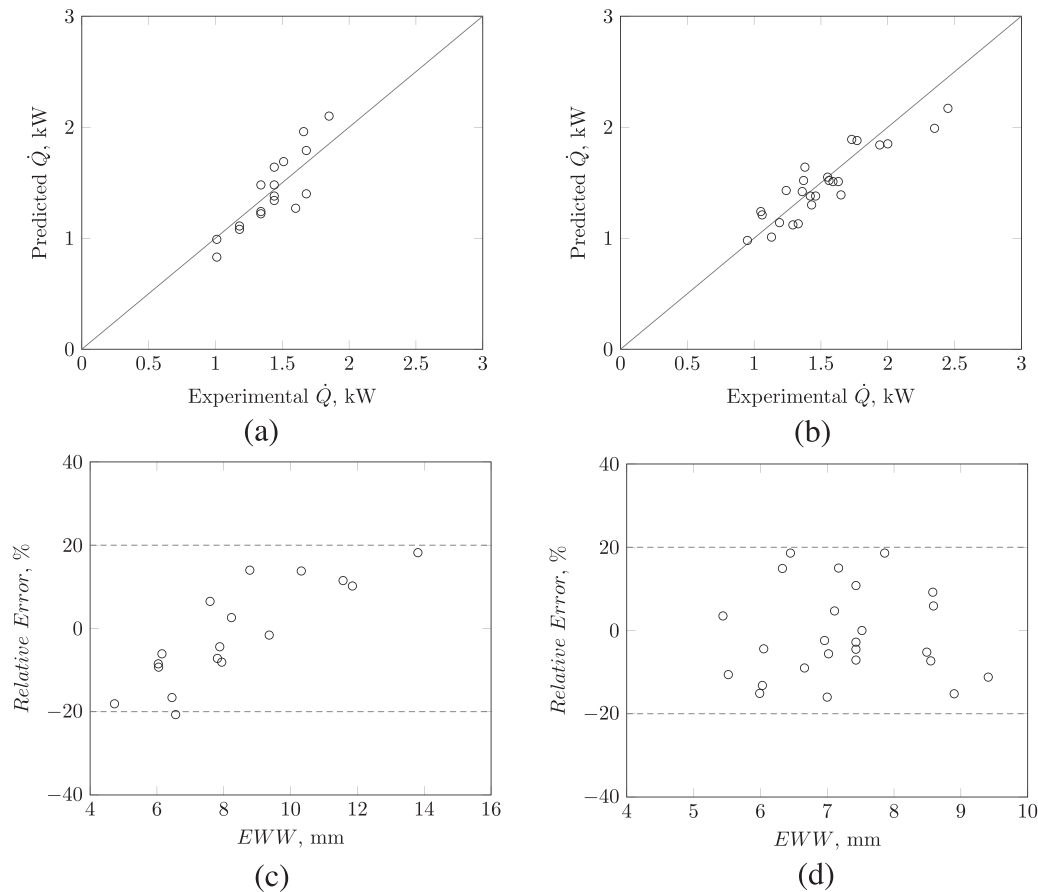


Fig. 9. Prediction of (a) average power and (c) relative error in power for P-TIG; and (b) average power and (d) relative error in power for plasma.

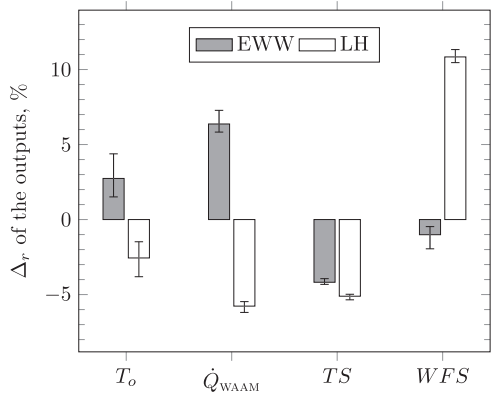


Fig. 10. Relative change in deposit dimensions, due to 10% increase in process parameters. Note that the error bars indicate the maximum and minimum values.

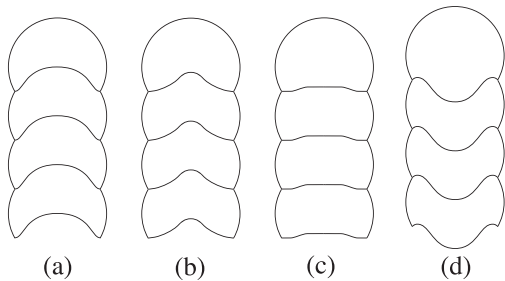


Fig. 11. Possible fusion profiles in AM.

Table 3		
Process set points for the comparison of arc power in PTA (see Fig. 4a and b).		
	Fig. 4a	Fig. 4b
Settings		
Current, A	120	167
PGFR, L min ⁻¹	5.00	0.80
Output		
Arc voltage, V	23.3	21.6
Arc power, kW	2.77	3.63
LH, mm	1.62	1.59
EWW, mm	7.17	7.43

For instance, to demonstrate the differences in machine output that can occur in plasma WAAM, consider the two sets of parameters defined in Table 3 which both produce very similar deposit dimensions and are shown in Fig. 4. The travel and wire feed speeds were identical for the two conditions. Then, the similarity in average deposit dimensions, despite the difference in power is likely to be a consequence of either a different thermal efficiency and/or convection effects in the weld pool. The condition with the lower current has a higher plasma gas flow rate, which resulted in more than 850 W lower power consumption, as machine output. The weld pool for this condition (Fig. 4b) has a more pronounced molten pool depression.

Fuerschbach [31] observed that high penetration processes such as plasma welding produce greater melting efficiencies than low penetration processes such as TIG, i.e. the molten zone has a larger cross section for a given amount of energy input per unit length. To illustrate this, Fig. 11 shows possible weld pool profiles during AM for different processes according to [17,31] and WAAM. The different weld pool profiles are drawn from plasma deposition of Ti-6Al-4V WAAM

(Fig. 11a) which if etched correctly allows observation of the fusion zone, autogenous TIG (Fig. 11b) and plasma welding (Fig. 11c) of stainless steel and laser direct metal deposition of stainless steel (Fig. 11d). These differences, possibly due to different power densities may change the cross-sectional areas of molten material and hence may affect the precision of the power predicted by the model.

5. Conclusions

- A simple model was proposed that related the process parameters to the deposit geometry for Ti-6Al-4V WAAM deposits and was validated with experimental data. The approach is based on an analytical heat flow model and capillarity theory.
- Capillarity theory predicted that deposits with a radii equal to or below 6 mm were cylindrical in shape for Ti-6Al-4V due to surface tension forces dominating over the hydrostatic pressure. This prediction was supported by experimental evidence.
- The model was able to predict the weld power with an accuracy of $\pm 20\%$ in pulsed TIG and plasma WAAM and is useful for a first estimate of the power requirements to obtain a particular geometry. It also provides insight into how and why the input parameters affect process outputs such as the layer height and wall width.
- Using the model, it was possible to determine the sensitivity of the geometry to different input parameters. Even though the outputs are not particularly sensitive to the workpiece temperature, this parameter is difficult to control during production and could therefore lead to significant geometry variations.
- Conditions which produced the same deposit geometry, but with very different process parameters were explored. Parameters that result in a molten pool depression required lower power which could be due to greater melting efficiency, convection effects or a combination of the two.

Acknowledgements

The research presented above was funded partially by the National Commission for Scientific and Technological Research CONICYT, from the Chilean Ministry of Education, through the Doctoral scholarship program; and by the WAAM-Mat research program of Cranfield University.

References

- [1] S.W. Williams, F. Martina, A.C. Addison, J. Ding, G. Pardal, P. Colegrove, Wire + arc additive manufacturing, *Mater. Sci. Technol.* (2015) 641–647.
- [2] D. Rosenthal, Mathematical theory of heat distribution during welding and cutting, *Weld. J.* 20 (5) (1941) 220s–234s.
- [3] N. Rykalin, Teplovyy Osnovy Svarki-Chast' Pervaya: Protessy Rasprostraneniya Tela pri Dugovoy Svarkye (The Thermal Basis of Welding – Part 1: Diffusive Processes during Arc Welding), Academy of Sciences USSR, 1947 (in Russian).
- [4] N. Nguyen, Thermal analysis of welds, in: J.A. Goldak, M. Akhlaghi (Eds.), *Computational Welding Mechanics*, 1st ed., Springer Science + Business Media, LLC, New York, 2005, p. 322.
- [5] J. Elmer, W. Giedt, T.W. Eagar, The transition from shallow to deep penetration during electron beam welding, *Weld. J.* 69 (5) (1990) 167s–176s.
- [6] C. Heiple, J. Roper, The geometry of gas tungsten arc, gas metal arc, and submerged arc weld beads, in: D.L. Olson, R. Dixon, A.L. Liby (Eds.), *Welding: Theory and Practice*, North-Holland, Amsterdam, 1990, p. 389 (Chapter 1).
- [7] N. Malmuth, W. Hall, B. Davis, C. Rosen, Transient thermal phenomena and weld geometry in GTAW, *Weld. J.* 53 (9) (1974) 388s–400s.
- [8] N. Malmuth, Temperature field of a moving point source with change of state, *Int. J. Heat Mass Transfer* 19 (1976) 349–354.
- [9] N. Christensen, V. del Davies, K. Gjermundsen, Distribution of temperatures in arc welding, *Br. Weld. J.* 12 (2) (1965) 54–75.
- [10] A. Vasinonta, J.L. Beuth, M.L. Griffith, A process map for consistent build conditions in the solid freeform fabrication of thin-walled structures, *J. Manuf. Sci. Eng.* 123 (4) (2001) 615–622.
- [11] A. Vasinonta, J.L. Beuth, M. Griffith, Process maps for predicting residual stress and melt pool size in the laser-based fabrication of thin-walled structures, *J. Manuf. Sci. Eng.* 129 (1) (2007) 101–109.
- [12] A. Traidia, F. Roger, E. Guyot, J. Schroeder, G. Lubineau, Hybrid 2D-3D modelling of GTA welding with filler wire addition, *Int. J. Heat Mass Transfer* 55 (15–16) (2012) 3946–3963.
- [13] S.H. Kang, H.S. Cho, Analytical solution for transient temperature distribution in gas tungsten arc welding with consideration of filler wire, *Proc. Inst. Mech. Eng. Part B: J. Eng. Manuf.* 213 (8) (1999) 799–811.
- [14] P.S.P. Myers, O.A.O. Uyehara, G.L. Borman, Bulletin 123. Fundamentals of Heat Flow in Welding, Welding Research Institute, London, 1967.
- [15] P.W. Fuerschbach, Melting efficiency in fusion welding, *The Metal Science of Joining*, (1992), pp. 21–29.
- [16] A. Wells, Heat flow in welding, *Weld. J.* 31 (5) (1952) 263s–267s.
- [17] A.J. Pinkerton, L. Li, Modelling the geometry of a moving laser melt pool and deposition track via energy and mass balances, *J. Phys. D: Appl. Phys.* 37 (2004) 1885–1895.
- [18] J.L. Beuth, N.W. Klingbeil, The role of process variables in laser-based direct metal solid freeform fabrication, *JOM* 53 (9) (2001) 36–39.
- [19] X. Shan, M. Tan, N. O'Dowd, Developing a realistic FE analysis method for the welding of a NET single-bead-on-plate test specimen, *J. Mater. Process. Technol.* 192–193 (2007) 497–503.
- [20] E. Soylemez, J.L. Beuth, K.M. Taminger, Controlling melt pool dimensions over a wide range of material deposition rates in electron beam additive manufacturing, *Annual International Freeform Fabrication Symposium* (2010) 571–582.
- [21] F. Martina, J. Mehnert, S. Williams, P. Colegrove, F. Wang, Investigation of the benefits of plasma deposition for the additive layer manufacture of Ti-6Al-4V, *J. Mater. Process. Technol.* 212 (6) (2012) 1377–1386.
- [22] F. Martina, Investigation of methods to manipulate geometry, microstructure and mechanical properties in titanium large scale Wire + Arc Additive Manufacturing (Ph.D. thesis), Cranfield University, 2014.
- [23] V.R. Ryabov, G.F. Deyev, Surface Phenomena in Welding and Surfacing, E.O. Paton Electric Welding Institute, Kyiv, 1998.
- [24] P.-G. de Gennes, F. Brochard-Wyart, D. Quere, Capillarity and Wetting Phenomena - Drops, Bubbles, Pearls, Waves, 1st ed., Springer-Verlag, New York, 2004.
- [25] G.F. Deyev, D.G. Deyev, Surface Phenomena in Fusion Welding Processes, 1st ed., CRC Press, Boca Raton, FL, 2006.
- [26] G. Voloshkevich, Welding vertical joints by forced formation, Jubilee Collection Dedicated to the 80th Anniversary of Paton, Publishing House of the USSR Academy of Sciences, Kiev, 1951, pp. 371–395.
- [27] B. Berezovskii, V. Stikhin, Influence of forces of surface tension on formation of reinforcement of weld, *Weld. Prod.* (1) (1977) 51–53.
- [28] P.S. Almeida, Process control and development in wire and arc additive manufacturing (Ph.D. thesis), Cranfield University, 2012.
- [29] R.K. Wunderlich, Surface tension and viscosity of industrial Ti-alloys measured by the oscillating drop method on board parabolic flights, *High Temp. Mater. Processes* (London) 27 (6) (2008) 401–412.
- [30] A.R. McAndrew, Modelling of Ti-6Al-4V linear friction welds (Ph.D. thesis), Cranfield University, 2015.
- [31] P.W. Fuerschbach, G.A. Knorovsky, A study of melting efficiency in plasma arc and gas tungsten arc welding, *Weld. J.* 70 (11) (1991) 287s–297s.
- [32] N. Stenbacka, I. Choquet, K. Hurtig, Review of arc efficiency values for gas tungsten arc welding, *Soldagem e Inspecao* 18 (12) (2013) 380–390.